

PHYSICOCHEMICAL PROCESSES  
AT THE INTERFACES

Scanning Tunneling Microscopic and Scanning Tunneling Spectroscopic Studies of Nanostructure and Surface Energy Properties of Stainless Steel #Kh18N10T. 1. Measurements at Interfaces with Air and 0.1 N HCl solution

Yu. M. Stryuchkova and E. V. Kasatkin

Karpov Institute of Physical Chemistry, ul. Vorontsovo pole 10, Moscow, 105054 Russia

Received November 7, 2007

**Abstract**—Stainless steel #Kh18N10T is studied by electrochemical scanning tunneling microscopy (ESTM) and electrochemical scanning tunneling spectroscopy (ESCS) methods at the interface with air and for the fixed sample and probe potentials in 0.1 N HCl. Local spectral dependences of tunneling current on the tunneling voltage ( $I_t, U_t$ ) are studied in either air or solution in the vicinity of potentials corresponding to stable properties. The local tunneling conductivity ( $G_o$ ), the coefficient of the probability of tunneling transfer of an electron to the tip ( $\alpha$ ), and the logarithmic-dependence slope ( $\beta = U_t/\ln(I_t)$ ) are calculated. As for Fe–Cr alloys, it is shown that at the atomic level, the local energy properties of a steel #Kh18N10T are determined by the mutual effect of neighboring atoms (the matrix effect).

PACS numbers: @@@@

DOI: 10.1134/S0033173208050020

INTRODUCTION

Steel #Kh18N10T pertains to an abundant group of chromium–nickel austenitic corrosion-resistant steels known in the world practice as “steels of the 18-10 type”.

Examples are known where scanning tunneling microscopy (STM) was used in studying the nanomorphology of steel surface, which included the STM study of the air-exposed (100) face of a Fe–18Cr–13Ni alloy single crystal [1]. It was found that a passive film formed during the anodic polarization in 0.5 M H<sub>2</sub>SO<sub>4</sub> at +500 mV (NHE) had a layered structure with the external layer  $0.9 \pm 0.2$  nm thick consisting of  $96 \pm 2\%$  Cr(OH)<sub>3</sub> and  $4 \pm 2\%$  Ni(OH)<sub>2</sub>. The inner layer  $1.1 \pm 0.2$  nm thick consisted of 18% Fe<sub>2</sub>O<sub>3</sub> and 82%  $\alpha$ -Cr<sub>2</sub>O<sub>3</sub>. Using STM measurements, the passive-film morphology was examined to reveal 50–100 nm grains; at high resolution, the atomic nanostructure with characteristic distances of 0.298 and 0.261 was observed.

In this study, the local electrophysical properties of the steel surface that determine its corrosion behavior were studied by a combination of methods of scanning tunneling spectroscopy (STS) and scanning tunneling microscopy including its electrochemical version (ESTM).

The STM and ESTM instruments make it possible to carry out local measurements of the  $I_t$  vs.  $U_t$  dependence in selected sites of the scanned surface region by recording spectra pertaining to the tunneling process on individual surface atoms and performing their quantita-

tive analysis. These dependences are adequately described by the formula [2]

$$I_t = I_{oo} \{ \exp[\alpha U_t G_o / I_{oo}] - \exp[-(1 - \alpha) U_t G_o / I_{oo}] \}, \quad (1)$$

where  $I_{oo}$  is a non-zero tunneling electron-exchange current between the tip and the surface at  $U_t = 0$ ;  $G_o$  is the minimum tunneling conductivity for  $U_t = 0$ . Both these parameters depend on the tunneling gap determined by the maintained STM tunneling conductivity  $G_1 = I_o / U_{to}$ , where  $I_o$  and  $U_{to}$  are the fixed and stabilized STM tunneling current and tunneling voltage, respectively. The dimensionless coefficient  $\alpha$  reflects the asymmetry of probability of the tunneling electron transfer to the tip, which depends on physicochemical properties of a local site.

From Eq. (1), it is evident that for  $\alpha \rightarrow 1$ , the following relationships emerge:

$$U_t G_o / I_{oo} = \ln(I_t) - \ln(I_{oo}) \quad (2)$$

and

$$\beta = dU_t / d\ln(I_t) = I_{oo} / G_o, \quad (3)$$

where  $\beta$  is the maximum slope coefficient expressed in V (or mV) that reflects the tunneling activity of a particular site in an image. Substituting  $\beta G_o$  for  $I_{oo}$  in Eq. (1), we obtain relationship (4) that reflects the effect of  $\beta$  on  $I_t$

and relationship (5) that illustrates the effect of  $I_0$  and  $U_{t0}$  on  $I_t$

$$I_t = \beta G_o [\exp(\alpha U_t / \beta) - \exp(-(1 - \alpha) U_t / \beta)], \quad (4)$$

$$I_t = I_0 \beta / (U_{t0} \gamma) [\exp(\alpha U_t / \beta) - \exp(-(1 - \alpha) U_t / \beta)], \quad (5)$$

where  $\gamma = I_0 / (G_o U_{t0})$ .

It is evident that the tunneling current depends on both the minimum tunneling conductivity, which depends on the STM-sustained initial tunneling conductivity  $G_t$ , and coefficients  $\alpha$  and  $\beta$ , which are independent of the latter value and enter into Eqs. (4) and (5) not only as cofactors but also under the exponent as well.

### EXPERIMENTAL

We used an electrochemical scanning tunneling microscope (ESTM) of the "C3M Solver EC" type with the maximum scanning resolution of 0.022 nm. Measurements were carried out at room temperature using a local scanning tunneling spectroscopy mode with respect to voltage. The following ESTM experimental conditions were used:  $I_t = \text{const}$ ,  $I_0 = 0.1$  nA for the controlled sample and probe potentials at the tunneling voltage  $U_{t0} = 100$  mV.

As the reference electrode, a miniature silver-chloride electrode fixed in the ESTM cell was used; the counter electrode represented a Pt-Ir wire. Under experimental conditions, the sample and probe potentials were maintained by a bipotentiostat, which was a part of the C3M Solver EC setup developed at NT-MTD based on a IPC-TWIN bipotentiostat designed at ZAO "Kronas".

Probes for STM and STS measurements were prepared from Pt-Ir wire containing 25% Ir. The probe's tip, which was periodically immersed in solution, was insulated by a coating with Glassofor polymer applied by an electrochemical procedure. The quality of the tip was controlled by a test envisaged in this setup, namely, by measuring a spectroscopic dependence at the removal of the probe from a sample [3, 4].

In this work, samples of stainless steel #KH18N10T (68.9% Fe–17.8% Cr–10.4% Ni–0.52% Ti) were studied in air and at the interface with an electrolyte. The latter represented, as a rule, 0.01 N HCl solution prepared with twice distilled water. Samples of sheet steel (0.15 mm thick) were fixed in the elaborated miniature electrochemical cell of perfluorinated polymer. Prior to be placed into a cell for STM measurements, samples were polished with diamond powder to high luster, washed with acetone, ethanol, and, finally, twice distilled water. When the measurements were carried out in electrolyte solution, before an ESTM image was measured, the sample potential ( $E_s$ ) +100 mV and the

tip potential ( $E_t$ ) +200 mV were stabilized by the bipotentiostat.<sup>1</sup>

After an STM image was obtained, STS spectra were recorded, namely, series of  $I_t$  vs.  $U_t$  (in air) or  $I_{t,ex}$  vs.  $U_t$  (in solution) curves by moving a probe over the chosen surface area, as a rule, over a square net of 120 cells, where  $I_{t,ex}$  means the experimentally recorded current, which for experiments in solution corresponded to a sum of tunneling and faradaic currents ( $I_{t,ex} = I_t + I_{far}$ ). In this case, the tunneling voltage in each point varied from –0.4 to +0.8 V and back with the scanning rate  $U_t \pm 1$  V/s.

In the beginning and end of each ESTM experiment, a dependence of faradaic current on the uninsulated part of the withdrawn tip on its potential ( $E_t$ ) was recorded. This made it possible to obtain the corrected  $I_{t,ex}$  vs.  $U_t$  curve by subtracting this background faradaic current ( $I_{far}$ ) from the  $I_{t,ex}$  vs.  $U_t$  dependence using a specially developed program. The obtained data were processed using a computer program that allowed one to find  $I_{0o}$ ,  $G_o$ , and  $\alpha$  by minimizing the least square deviation between the experimental and calculated  $I_t$  values for each  $U_t$  in a curve.

### RESULTS AND DISCUSSION

Electrochemical characteristics of #Kh18N10T alloy in dilute acid solutions were determined by polarization measurements on its sample by using either an IPC-Pro-3A potentiostat or a bipotentiostat in an ESTM cell. The result obtained with both instruments did not show any principal differences. Below, the data measured in an ESTM cell are shown for a sample with the known surface area. Figure 1 demonstrates potentiodynamic polarization curves recorded with a potential scan rate of  $\pm 5$  mV/s in 0.01 N H<sub>2</sub>SO<sub>4</sub> (Fig. 1a) and 0.01 N HCl (Fig. 1b) solutions.

In [5, 6], polarization curves were measured on pure iron, chromium, and nickel in 0.1 N H<sub>2</sub>SO<sub>4</sub> solutions at 22°C and also on the #Kh18N10T alloy in boiling 3.4 N H<sub>2</sub>SO<sub>4</sub> solution. Results obtained by varying the potential from cathodic values corresponding to the active reduction of the metal surface were shown. Each curve had an active dissolution segment.

In the present study, the polarization measurements of the #Kh18N10T alloy at room temperature (Fig. 1), did not make the electrode be subjected to active cathodic polarization, and the cyclic polarization including multiple runs from cathodic to anodic potentials and back, revealed no active dissolution range for this alloy. Apparently, it was caused by sufficient passivity of the alloy surface exposed to air and the electrolyte of a low acidity. This state made the ESTM measurements be easier.

<sup>1</sup> The cell contained an Ag/AgCl reference electrode with a potential of 340 mV in 0.01 N HCl; in the text below, the potentials are shown on the NHE scale, i.e., a potential of +100 mV (Ag/AgCl) corresponds to +440 mV (NHE).

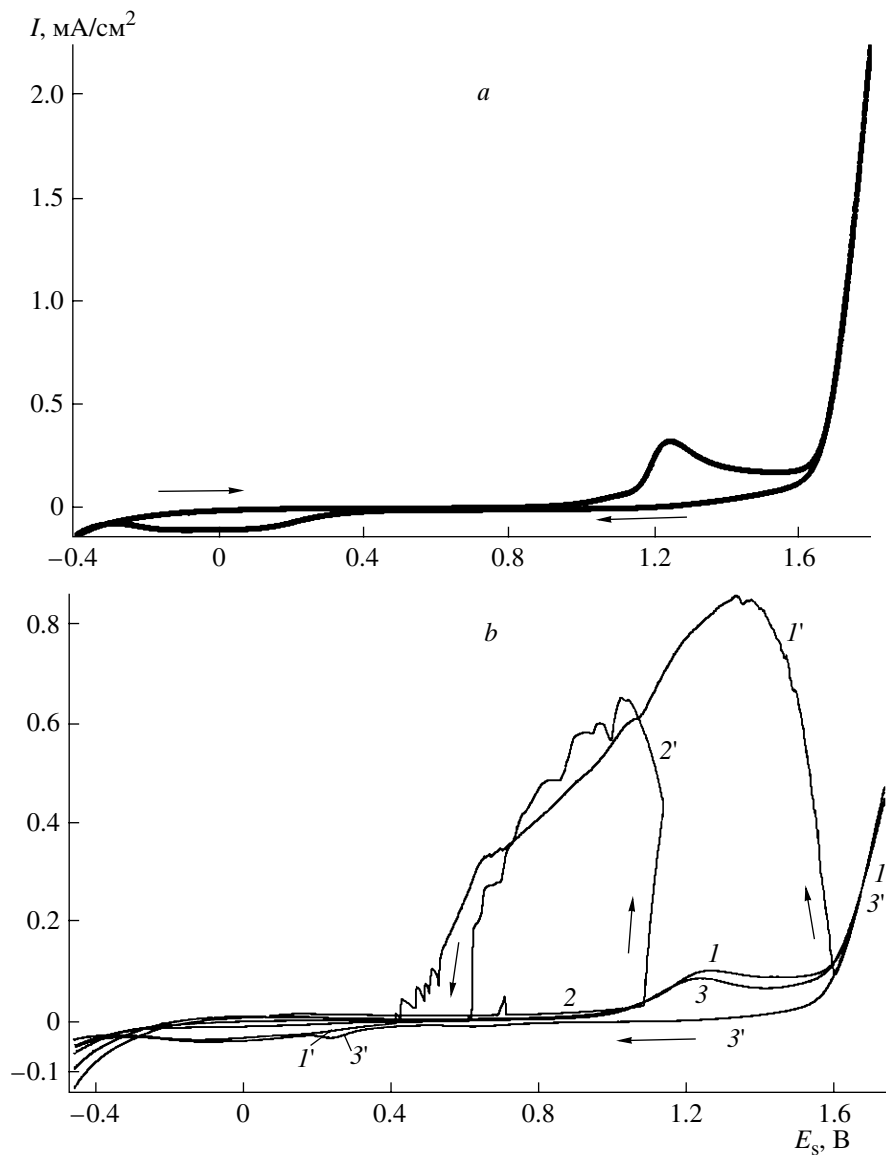


**Fig. 1.** Potentiodynamic polarization curves of stainless steel #Kh18N10T: (a) 0.01 N  $\text{H}_2\text{SO}_4$  solution, (b) 0.01 N HCl solution; (1, 2 and 1', 2') curves of the first cycle; (3, 3') curves of the 3rd cycle. Potential scan rate: (1, 2, 3) +5 mV/s, (1', 2', 3') -5 mV/s.

In a potential range under study, in dilute  $\text{H}_2\text{SO}_4$  and HCl solutions, the reverse polarization curves demonstrated a hysteresis reflecting the changes in the surface state with transients from cathodic processes on the alloy and from the initial states of its dissolution to the surface oxidation and passivation and, in the reverse run, to its reduction. A peak in the direct run in the vicinity of 1.25 V was associated with the selective dissolution of the titanium carbide admixture on the surface of this steel [5–7]. In the reverse run, a depression of cathodic current appeared in a potential range from +300 to -300 mV. For a shorter range of cyclic polarization (from -400 to +1200 mV), neither the peak associated with TiC dissolution in the direct run, nor the depression in the back run were observed. Apparently,

this cathodic current is associated with the  $\text{TiO}^{2+}$  reduction from the near-electrode solution layer.

A difference revealed between the measurement in 0.01 N HCl and  $\text{H}_2\text{SO}_4$  solutions was associated with the fact that in the hydrochloric acid solution, in a potential range from +405 to +1610 mV, in the first cycle, in its direct and, sometimes, back runs, a breakdown of the passive state and considerable surface dissolution with the formation of pits were observed. Apparently, due to the continued etching of pits, the anodic current increased further despite a decrease in the potential, passed through a maximum, and then decreased; the sample etching stopped only at +405 mV as seen in Fig. 1b, line 3. Such a breakdown was also observed in the curves recorded in 0.01 N HCl in a range from -400 to +1800 mV (Fig. 1b, curve 2). In the

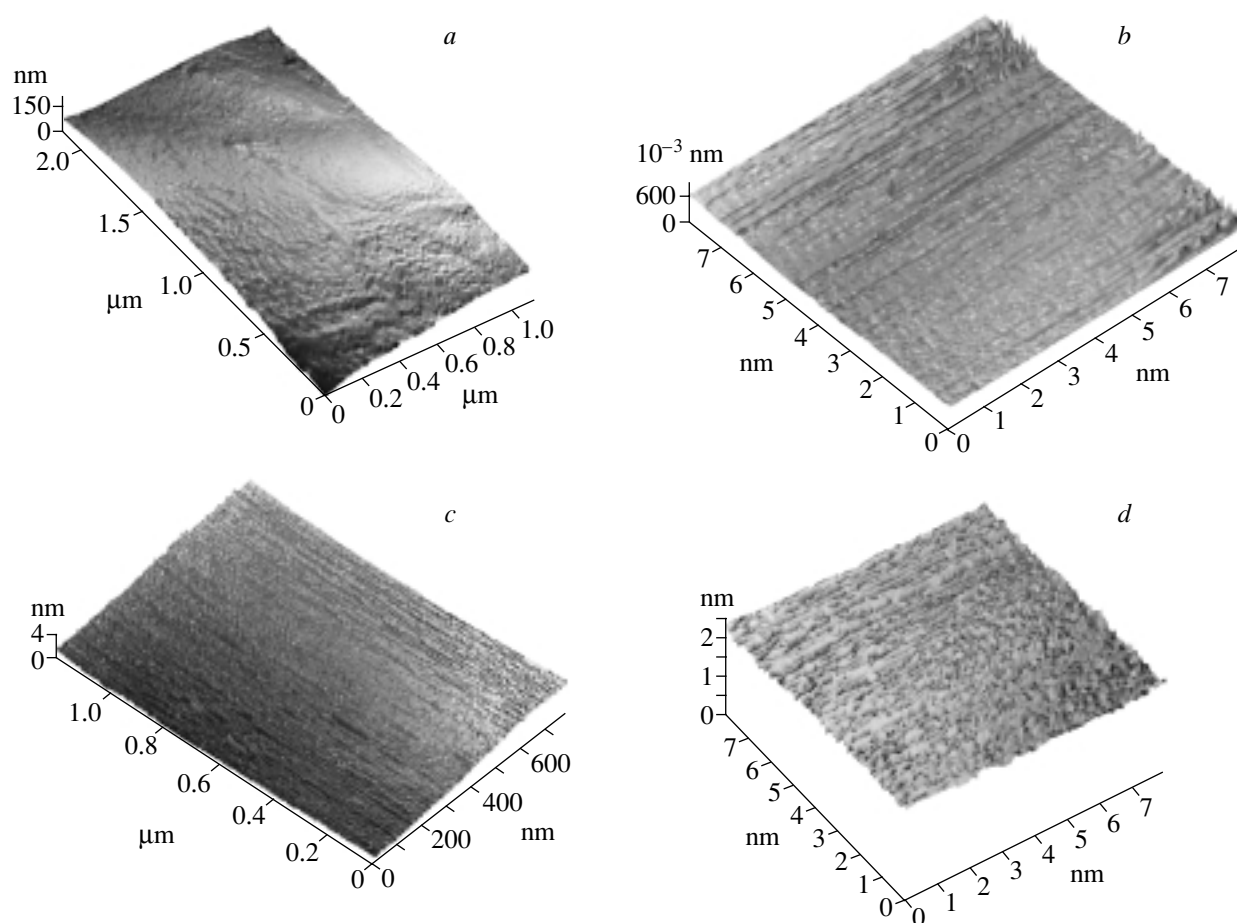


**Fig. 2.** Images of #Kh18N10T steel surface measured with Solver EC ESTM; (a,b) in air,  $U_t = 100$  mV,  $I_0 = 0.100$  nA; (c, d) in 0.01 N HCl solution at  $E_s = +440$  mV,  $U_t = 100$  mV,  $I_0 = 0.100$  nA; (a, c) low resolution: (a) scanning in steps of 9.945 nm, (c) scanning in steps of 4.683 nm; (b, d) high resolution (at atomic level): scanning in steps of 0.058 nm.

next polarization curve both in ranges from  $-400$  to  $+1200$  mV and from  $-400$  to  $+180$  mV, the breakdown disappeared and the direct and back curves gradually merged together. Pitting on the #Kh18N10T-type steel was already observed [8–14]; it was also noted that pits appeared due to the simultaneous presence of chloride ions as depassivators and an oxidant, particularly, oxygen, in solution. In chloride-free sulfate solutions, steel was so strongly passivated that no pits were formed.

Thus, in a hydrochloric acid solution, the stability range for steel #Kh18N10T, which could be conveniently studied by the ESTM technique, narrowed down to a range from  $-200$  to  $+950$  mV.

STM and ESTM measurements shown below were carried out at an open-circuit potential stabilized in a 0.01 N HCl solution at 100 mV in the 0.01 N HCl scale or  $+440$  mV in the NHE scale. Results obtained at other potentials will be shown in our next publications.

Figure 2 shows STM images of a sample of steel #Kh18N10T, measured in air (Figs. 2a and 2b), in 0.01 N HCl solution at  $E_s = +440$  mV (Figs. 2c, 2d). The electronic profile image of the steel #Kh18N10T surface in

air, is shown in Fig. 2a on a field of  $2.5 \times 1 \mu\text{m}$ . Its relief, reaches 140 nm, which corresponds to approximately  $\sim 5\%$  roughness of micrograins.

However, at high magnifications of tunneling microscope as, e.g., in Fig. 2b that spans nearly  $10^3$  atoms ( $8 \times 8$  nm field), where only one face of a microcrystal is covered by the scanned field. The surface looks virtually atomically smooth with the height difference of merely 0.6 nm, which does not exceed two atomic layers. Note that in the vast majority of measurements on polycrystalline samples at high magnification, where the field did not exceed  $0.01 \mu\text{m}^2$ , STM measurements allow one to select and visualize atomically smooth faces of single crystals.

Figure 2c shows ESTM images of steel #Kh18N10T in 0.01 N HCl solution for the scanned field of  $1 \times 0.8 \mu\text{m}$  and the sample potential of  $+440$  mV. These images are much smoother with the height difference not exceeding 3 nm. The high-resolution ( $8 \times 8$  nm) ESTM image shown in Fig. 2d is also atomically smooth as in air.

Local spectral dependences of the tunneling current on the tunneling voltage ( $I_t$  vs.  $U_t$ ) in solution at the con-

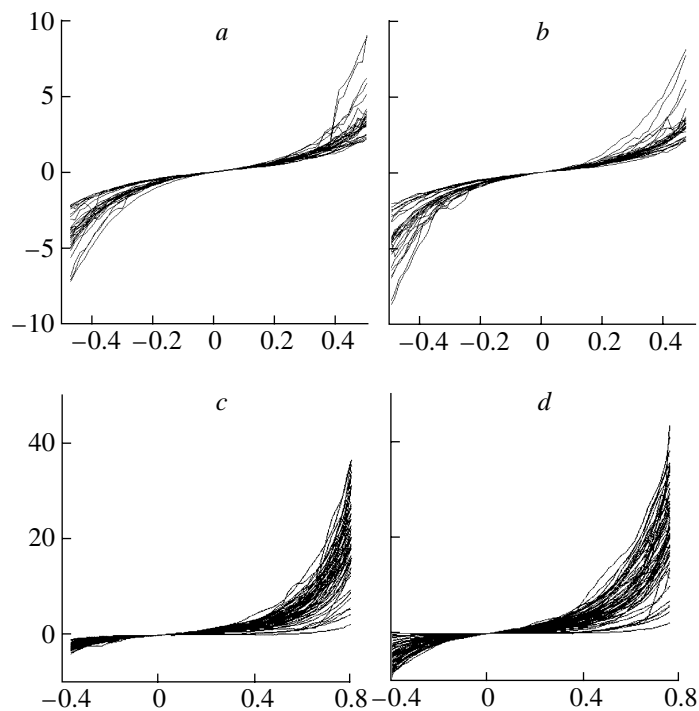


**Fig. 3.** Spectra of  $I_t$  vs.  $U_t$  dependence, measured on steel #Kh18N10T (a, b) in air and (c, d) in 0.01 N HCl solution; (a, c)  $dU_t/d\tau > 0$ , (b, d)  $dU_t/d\tau < 0$ .

trolled sample and probe potentials on stainless-steel samples were studied after recording an STM image. As an example, Fig. 3 shows the typical tunneling current vs. tunneling voltage ( $I_t$  vs.  $U_t$ ) dependences for #Kh18N10T measured in air and 0.1 N HCl solution. Figures 3a and 3b demonstrate  $I_t$  vs.  $U_t$  curves measured in air in an experiment which included recording 15 curves along each of two image diagonals (30 curves in total) with a step of  $\sim 90$  nm between the sites of measurements. It is seen that for both direct (3a) and reverse (3b) curves, there exists a sufficiently large number of closely located curves that reflect the average surface state. At the same time, there are curves with different slopes that point to both higher and lower tunneling activity of the local sites. Figure 3c and 3d show spectra of  $I_t$  vs.  $U_t$  curves (60 spectra for each of 120 curves) corrected for the faradaic current, which were measured by moving “along the net” with a step of 133 nm on a sample in 0.01 N HCl. It is evident that sufficiently wide deviations are observed between the local  $I_t$  vs.  $U_t$  dependences, which were associated with the non-equivalent tunneling activity of different surface sites, despite the same potential. This is reflected in the parameters  $\alpha$ ,  $\beta$ , and  $\gamma = G_0/G_1$ .

Based on a set of  $I_t$  vs.  $U_t$  dependences for steel #Kh18N10T, for each of 1429 analyzed curves, the values of local tunneling conductivity  $G_0$ , tunneling exchange current  $I_{00}$ , and coefficients  $\lambda$ ,  $\beta$ , and  $\gamma$  were calculated. The average values of these parameters

reflected the mean tunneling surface activity while their variation characterized the extent of their difference.

To illustrate these properties, Figs. 4 and 5 show histograms for measurements in air and at a potential of +440 mV in 0.01 M HCl (Fig. 6), plotted with taking into account the weight factors of measured values. The data that did not fit the length of the histogram partition could be designated by a peak in the beginning and the end of the whole sampling area, as seen in certain histograms.

In similar measurements performed earlier on Fe–Cr alloys [15], it was shown that histograms of the distribution of local  $\alpha$ ,  $\beta$ , and  $\gamma$  values substantially differ both between iron and chromium, as well as their alloys with different Fe and Cr contents, which is due to the structure of their lattices. Comparing the data obtained for #Kh18N10T alloy in air with analogous histograms for alloys with the same content of chromium (Fe–17.4Cr) or iron (Fe–27%Cr) (Fig. 4) demonstrates a substantial difference in parameters, which is most probably explained by the presence of a new component, nickel, in #Kh18N10T alloys.

In contrast to the Fe–Cr alloys under comparison, in which the distribution of  $\alpha$  had a pronounced shoulder for  $\alpha = 0.46$  and peaks in the vicinity of  $\alpha = 0.49$ , for steel #Kh18N10T, the dominating (by more than 10%) peak at 0.47 V and a smaller peak at  $\alpha = 0.49$  V were observed. For steel #Kh18N10T, histograms of  $\beta$  distribution that reflect the maximum slope  $U_t/\ln(I_t)$  did not coincide with analogous distribution for Fe–Cr alloys,

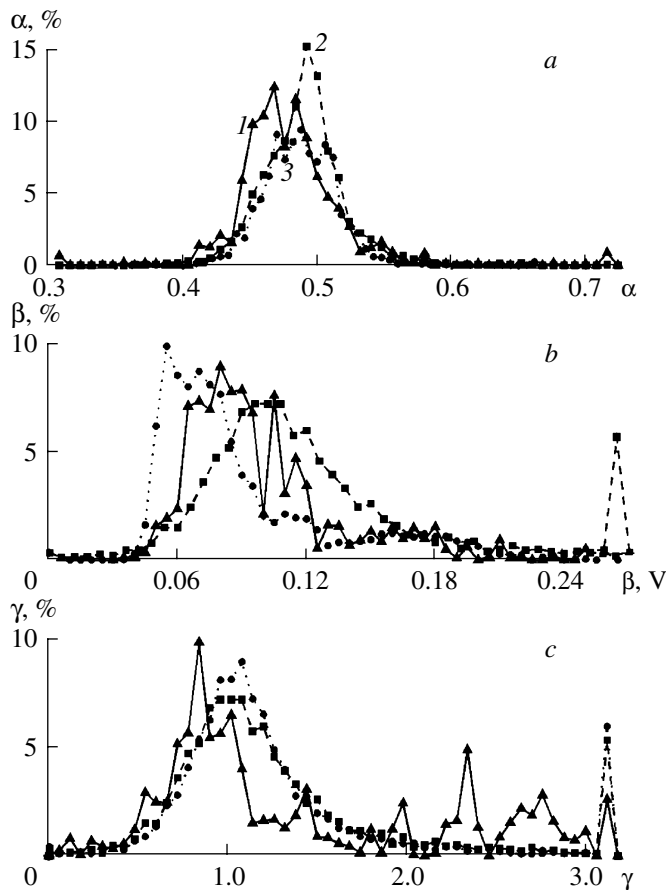


**Fig. 4.** Distribution of values of parameters describing the behavior of tunneling current on the surface during the air-induced changes in properties of steel #Kh18N10T and Fe–Cr alloys;  $dU_t/dt > 0$ : (a) coefficient of probability of electron tunneling transfer from a sample to the tip ( $\alpha$ ); (b) slope of logarithmic dependence  $U_t/\ln(I_t) - (\beta)$ ; (c) ratio of local ( $G_0$ ) to preset ( $G_1$ ) conductivity ( $\gamma$ ); (1) steel #Kh18N10T, (2) alloy 72.2%Fe–27.8%Cr, (3) alloy 82.6%Fe–17.

namely the maximum fell to a value  $\beta = 80$  mV. Whereas for Fe–Cr alloys, the distribution histograms of a parameter  $\gamma$  (that characterizes the local field activity) had a clear maximum for  $\gamma = 1$  and nearly 5% of active sites (for  $\gamma > 3$ ), for steel #Kh18N10T, besides a peak at  $\gamma = 1$ , there were several smaller peaks of enhanced activity for  $\gamma = 1.44, 1.98, 2.34, 2.76$ , respectively.

Thus, as in the case of Fe–Cr alloys, we observed that despite its complex nature, steel #Kh18N10T reveals no individual tunneling properties for Fe, Cr, or Ni surface atoms. Apparently, the recorded properties of steel are determined by the mutual effect of its components, the presence of the matrix effect; this result is apparently of fundamental value for nanoproperties of the alloys.

Figure 5 compares histograms for alloy #Kh18N10T, in which the distributions of parameters  $\alpha$ ,  $\beta$  and  $\gamma$  were

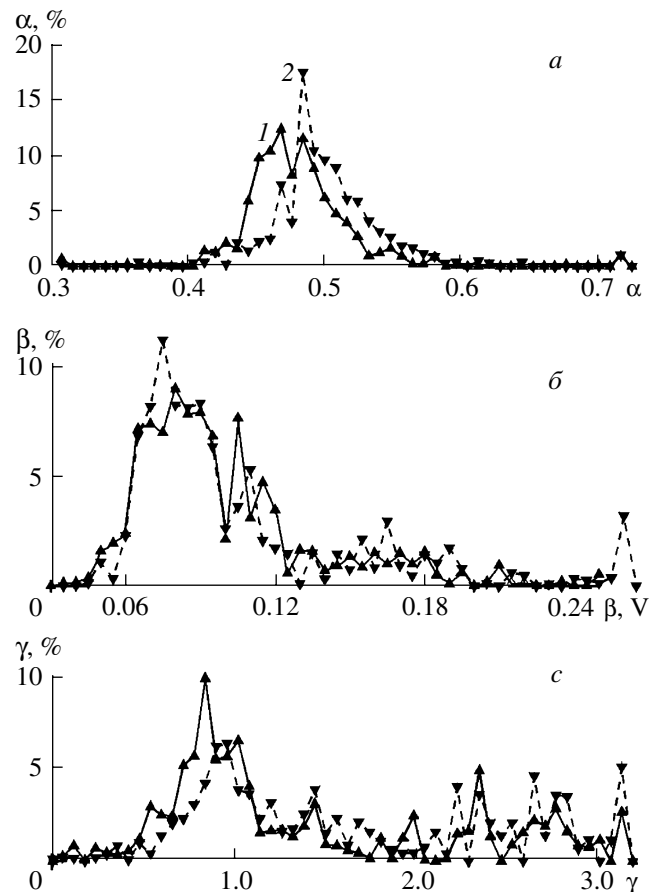


**Fig. 5.** Distribution of values of parameters describing the behavior of tunneling current on the surface of #Kh18N10T steel in air: (a) coefficient of probability of electron tunneling transfer from a sample to the tip ( $\alpha$ ); (b) slope of logarithmic dependence  $U_t/\ln(I_t) - (\beta)$ ; (c) ratio of local ( $G_0$ ) to preset ( $G_1$ ) conductivity ( $\gamma$ ); (a,c)  $dU_t/dt > 0$ , (b, d)  $dU_t/dt < 0$ .

calculated not only in scans with  $dU_t/dt > 0$  (358 curves) but also in reverse scans (351 curves). The recorded differences are associated with the fact that the surface state somewhat changed when an electron was transferred to the tip and from it. These changes largely concerned the coefficient  $\alpha$  that reflects the probability of electron transfer from a sample to the tip.

Figure 6 shows histograms of the dependences of  $\alpha$ ,  $\beta$ , and  $\gamma = G_0/G_1$  for  $G_1 = 1.0$ , which were obtained by processing 360 direct curves and the equal number of reverse curves for ESTM measurements in 0.01 N HCl at the sample potential of +440 mV<sup>2</sup>.

<sup>2</sup> Insofar as the measurements on alloys of the Fe–Cr system were carried out only in air and for the overwhelming majority of cases for  $dU_t/dt > 0$  scans, it is impossible to compare our data with the local surface properties of Fe–Cr alloys in acidic solutions including the scans with  $dU_t/dt < 0$ .

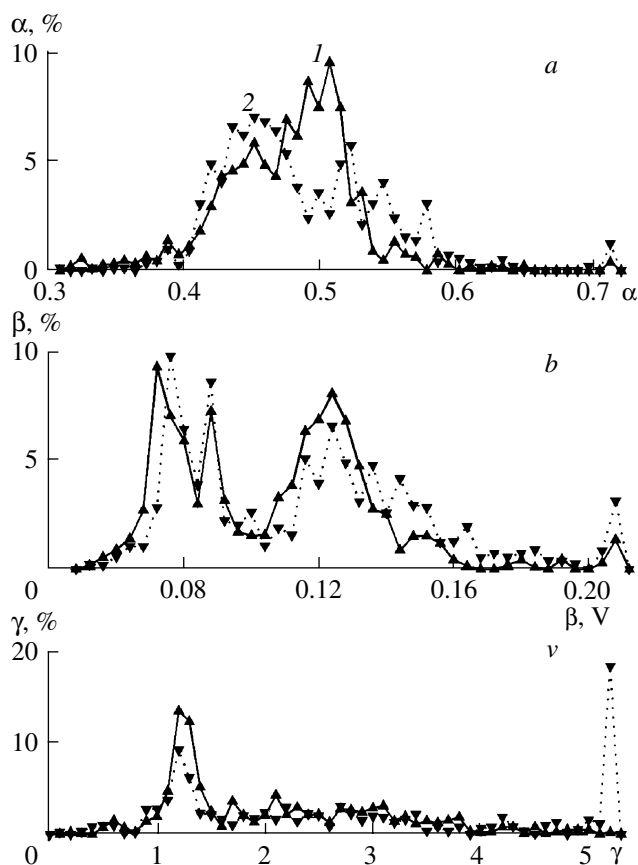


**Fig. 6.** Distribution of values of parameters describing the behavior of tunneling current on the surface of #Kh18N10T steel in 0.01 HCl solution: (a) coefficient of probability of electron tunneling transfer from a sample to the tip ( $\alpha$ ); (b) slope of logarithmic dependence  $U$  vs.  $\ln(I_t)$  ( $\beta$ ); (c) ratio of local ( $G_0$ ) to preset ( $G_1$ ) conductivity ( $\gamma$ ); (a,c)  $dU_t/d\tau > 0$ , (b, d)  $dU_t/d\tau < 0$ .

The same as for measurements in air, certain differences between histograms obtained at  $dU_t/d\tau > 0$  and  $dU_t/d\tau < 0$  could be distinguished; these differences were more pronounced for coefficient  $\alpha$ .

Comparing Figs. 5 and 6, shows that the distribution histograms of parameters under question, which were calculated from the data acquired in measurements in 0.01N HCl solution for a sample at a potential of +440 mV (Fig. 6) differ from analogous histograms in air (Fig. 5). Thus in solution, parameter  $\beta$  had pronounced peaks in both direct and back runs not only at 70–90 mV as in air but at 120 mV; the latter maximum was absent in air. Whereas for steel #Kh18N10T in air, the peak shifted to  $\gamma < 1$  and was less pronounced, the histograms of  $\gamma$  distribution in solution demonstrated a pronounced peak at  $\gamma = 1.2$ , which was dominant. This

SPELL: 1. austenitic, 2. nanoproperties

suggests that the local surface properties at the controlled potential and the other conditions equal are more stable, namely, the tunneling conductivity was more pronounced and had two characteristic  $\beta$  slopes; the probability factor of tunneling transfer  $\alpha$  for spectra of direct and reverse  $I_t$  vs.  $U_t$  dependences demonstrated still more pronounced differences due to the changes in the tip potential as a result of spectral measurements that reached the range of oxygen chemisorption.

Thus, the electrochemical scanning tunneling spectroscopy was used for the first time to study the local properties (on the atomic level) of stainless steel.

#### ACKNOWLEDGEMENTS

This study was financially supported by the Russian Foundation for Basic Research (grant no. 04-03-32337).

#### REFERENCES

1. Maurice, V., Yang, W.P., and Marcus, P., *J. Electrochem. Soc.*, 1998, vol. 145, no. 3, p. 909.
2. Kasatkin, E.V., Reznik, M.F., and Neburchilova, E.B., *Elektrokhimiya*, 2003, vol. 39, no. 3, p. 265.
3. Halbritter, J., Repphun, G., Vinzelberg, S., et al., *Electrochim. Acta*, 1995, vol. 40, p. 1385.
4. Kasatkin, E.V. and Neburchilova, E.B., *Elektrokhimiya*, 1998, vol. 34, no. 10, p. 1154.
5. Knyazheva, V.M., Sumakova, I.S., Kolotykin, Ya.M., and Kruzhkovskaya, A.A., *Zashch. Met.*, 1966, vol. 2, p. 628.
6. Kolotykin, Ya.M. and Knyazheva, V.M., *Itogi Nauki Tekhn., Ser. Korr. Zashch. Korr.*, Moscow: VINITI, 1974, vol. 3, p. 5.
7. Knyazheva, V.M., Chigal, V., and Kolotykin, Ya.M., *Zashch. Met.*, 1975, vol. 11, no. 5, p. 531.
8. Logan, H.L., *Korroziya metallov pod napryazheniem* (Stress Corrosion of Metals), Moscow: Metallurgiya, 1970.
9. Gagnolino, G. and Macdonald, D.D., *Corrosion*, 1982, vol. 38, no. 8, p. 408.
10. Bogoyavlenskii, V.L., *Korroziya staley na AES s vodnym teplonositelem* (Steel Corrosion at Nuclear Plants with Aqueous Coolant), Moscow: Energoatomizdat, 1984.
11. Garner, A., *Corrosion Australian*, 1988, vol. 13, no. 1, p. 16.
12. Burlov, V.V., Parputs, I.V., and Parputs, T.P., *Vestn. UDGU, Ser. Khim., Izhevsk*, 2005, no. 8, p. 3.
13. Parputs, T.P., *Cand. Sc. (Chem.) Dissertation*, Perm, 2007.
14. Mal'tseva, G.N., *Korroziya i zashchita oborudovaniya ot korrozii* (Corrosion and Corrosion Protection of Equipment), Penza: PGU, 2001.
15. Trofimova, E.V., Kasatkin, E.V., and Reformatskaya, I.I., *Zashch. Met.*, 2005, vol. 42, no. 3, p. 245.